JOURNAL OF SOLID STATE CHEMISTRY

Volume 179, Number 8, August 2006

CONTENTS

Thermal stability of high surface area silicon carbide materials

Piotr Krawiec and Stefan Kaskel

Page 2281

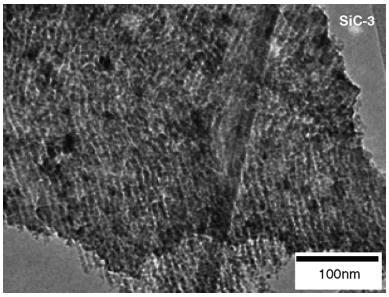

The synthesis of mesoporous silicon carbide by chemical vapor infiltration of dimethyl dichlorosilane into mesoporous silica SBA-15 and subsequent dissolution of the silica matrix was used for the preparation of mesoporous SiC with high specific surface areas up to $830\,m^2\,g^{-1}$ and pore sizes between 2 and 10 nm.

On the distribution of tetrelide atoms (Si, Ge) in $Gd_5(Si_xGe_{1-x})_4$

Sumohan Misra and Gordon J. Miller

Page 2290

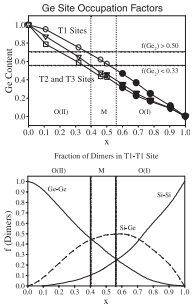

The Ge occupation in each T site in $Gd_5(Si_xGe_{1-x})_4$ is studied as a function of Si concentration, x. The different crystal structures are related to the fractions of Ge–Ge (solid), Si–Ge (dashed) and Si–Si (solid) dimers at the T1–T1 sites.

$M_{1-x}[W_2O_2X_6]$ with $M = K^+$, Tl^+, Ag^+, Hg^{2+}, Pb^{2+}; X = Cl, Br—A class of mixed valence tungsten (IV,V) compounds with layered structures, W–W bonds and high conductivity

Johannes Beck, Christian Kusterer, Rolf-Dieter Hoffmann and Rainer Pöttgen

Page 2298

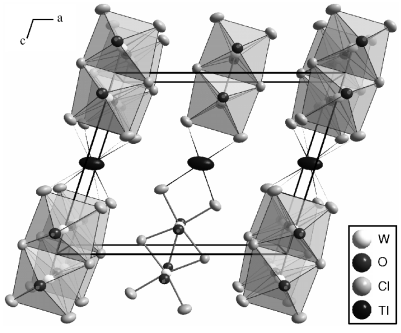

$WOCl_3$ has a particular reactivity to form non-stoichiometric quaternary compounds $M_{1-x}[W_2O_2Cl_6]$ with mono and divalent cations. The compounds exhibit temperature independent paramagnetism and high electrical conductivity.

Mn_5Si_3-type host-interstitial boron rare-earth metal silicide compounds RE_5Si_3: Crystal structures, physical properties and theoretical considerations

Jérome Roger, Mouna Ben Yahia, Volodymyr Babizhetskyy, Joseph Bauer, Stéphane Cordier, Roland Guérin, Kurt Hiebl, Xavier Rocquefelte, Jean-Yves Saillard and Jean-François Halet

Page 2310

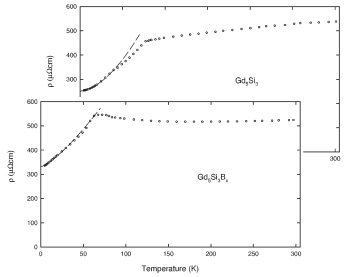

Incorporation of boron in vacant octahedral sites of the Mn_5Si_3-type phase Gd_5Si_3 modifies its resistivity properties.

Barrelane-like germanium clusters in Eu_3Ge_5: Crystal structure, chemical bonding and physical properties

Sergij Budnyk, Franz Weitzer, Christof Kubata, Yurii Prots, Lev G. Akselrud, Walter Schnelle, Kurt Hiebl, Reinhard Nesper, Frank R. Wagner and Yuri Grin

Page 2329

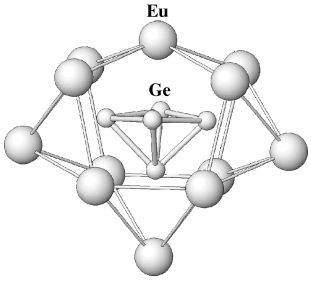

Main building blocks of the crystal structure Eu_3Ge_5 are $[Ge_5]^{6-}$ cluster anions surrounded by Eu^{2+} cations. The nearly tetragonal-pyramidal shape is suggested by the interatomic distances. Contrary to that, the bonding analysis with the ELF reveals only two- and three-bonded germanium atoms forming a strongly distorted [111]-barrelane-like cluster.

Synthesis and characterisation of hexagonal molybdenum nitrides

Alexey Yu. Ganin, Lorenz Kienle and Grigori V. Vajenine

Page 2339

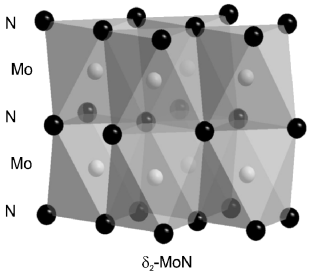

δ_2-MoN

Hexagonal δ_2-MoN with the NiAs-type crystal structure.

Continued

Regular Articles

Chemical shifts of atomic core levels and structure of $K_{1-x}Ti_{1-x}Sb_xOPO_4$, $x = 0$–0.23, solid solutions

V.V. Atuchin, O.A. Alekseeva, V.G. Kesler, L.D. Pokrovsky, N.I. Sorokina and V.I. Voronkova

Page 2349

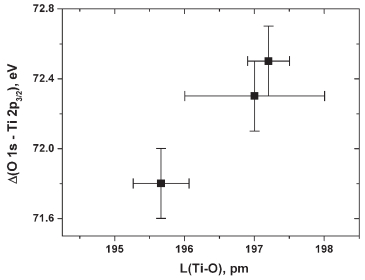

Dependence of Δ(O 1s–Ti 2$p_{3/2}$) on L(Ti–O) for KTP family crystals.

A novel blue-emitting phosphor $LiSrPO_4:Eu^{2+}$ for white LEDs

Z.C. Wu, J.X. Shi, J. Wang, M.L. Gong and Q. Su

Page 2356

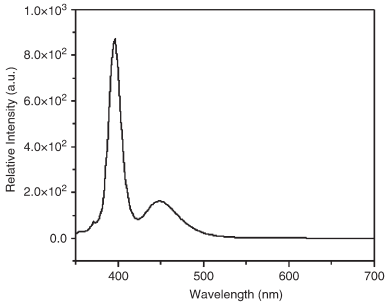

The EL spectrum of the blue LED-based $LiSrPO_4:Eu^{2+}$.

$PbI_4Cu_2(PPh_3)_4$: A heterometallic iodide with unusual *cis*-divacant octahedral coordination sphere for lead: Synthesis, structure, red-infrared fluorescence and theoretical studies

Le-Qing Fan, Yi-Zhi Huang, Li-Ming Wu, Ling Chen, Jun-Qian Li and En Ma

Page 2361

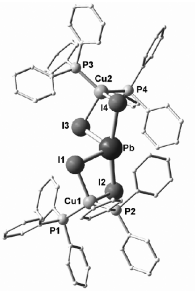

A new heterometallic iodide, $PbI_4Cu_2(PPh_3)_4$, was synthesized by reactions of PbI_2, CuI and triphenylphosphine (PPh_3) in DMF solution. The single-crystal X-ray diffraction analyses show that Pb(II) center adopts an unusual *cis*-divacant octahedral geometry. DFT calculations and fragment orbital interaction analyses reveal the presence of a 3c-4e hypervalent bonding about lead and the formation of the unusual *cis*-divacant $[PbI_4]^{2-}$ octahedron is energetically favorable. The title yellow compound has an optical bandgap of 2.69 eV and shows remarkable red-infrared fluorescence emission.

Regular Articles—Continued

Self-assembly of four new extended architectures based on reduced polyoxometalate clusters and cadmium complexes

Ying Ma, Yangguang Li, Enbo Wang, Ying Lu, Xinlong Wang and Xinxin Xu

Page 2367

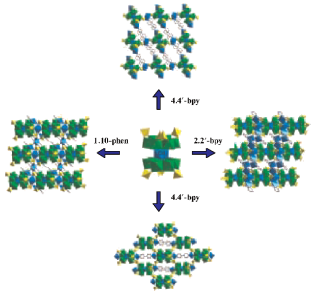

In this paper, we report four new extended architectures based on reduced polyoxometalate clusters and cadmium complexes. Compounds **1**–**4** are built of $Cd[P_4Mo_6]_2$ dimers as the basic structural motif and Cd–4,4′-bpy, Cd–phen and Cd–2,2′-bpy complexes as the linkers to constructed novel 2D layer structure.

Structural, magnetic, and spectroscopic studies of YAgSn, TmAgSn, and LuAgSn

C. Peter Sebastian, Hellmut Eckert, Constanze Fehse, Jon P. Wright, J. Paul Attfield, Dirk Johrendt, Sudhindra Rayaprol, Rolf-Dieter Hoffmann and Rainer Pöttgen

Page 2376

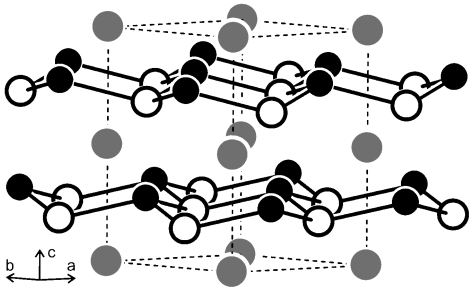

Crystal Structure of YAgSn.

Anion mediated polytype selectivity among the basic salts of Co(II)

T.N. Ramesh, Michael Rajamathi and P. Vishnu Kamath

Page 2386

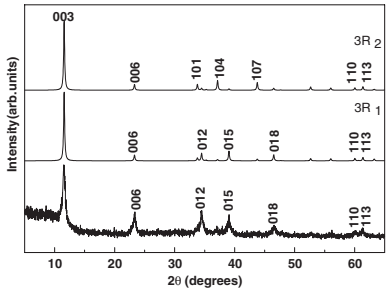

(a) Observed PXRD pattern of cobalt hydroxytartarate compared with the DIFFaX simulated patterns of (b) $3R_1$ and (c) $3R_2$ polytypes, respectively.

A crystallographic description of experimentally identified formation reactions of $Cu(In,Ga)Se_2$
F. Hergert, S. Jost, R. Hock and M. Purwins
Page 2394

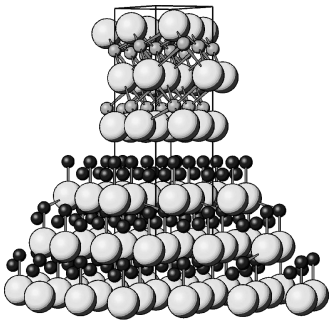

The epitaxial connection of the crystal structures of β-Cu_2Se (bottom) and β-In_2Se_3 (top) is the initiating step of one possible solid-state reaction for the formation of α-$CuInSe_2$.

A new anatase-type phase in the system Mg–Ta–O–N
H. Schilling, M. Lerch, A. Börger, K.-D. Becker, H. Wolff, R. Dronskowski, T. Bredow, M. Tovar and C. Baehtz
Page 2416

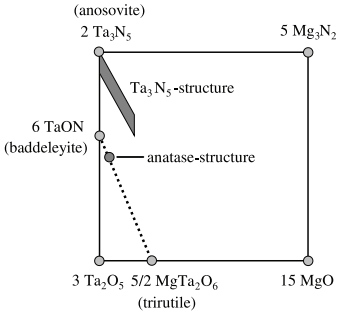

Schematic representation (constant 30 valencies) of all new compounds obtained as single phase samples in the system Mg–Ta–O–N (dark gray symbols).

Synthesis, structure and magnetic properties of porous magnetic composite, based on MCM-41 molecular sieve with Fe_3O_4 nanoparticles
Sergey V. Kolotilov, Oleksiy Shvets, Olivier Cador, Natalia Kasian, Vyacheslav G. Pavlov, Lahcène Ouahab, Vladimir G. Ilyin and Vitaly V. Pavlishchuk
Page 2426

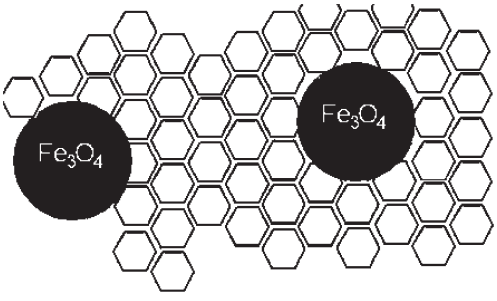

Schematic presentation of MCM-41/Fe_3O_4 composite.

A novel Mo(V) oligophosphate built up of di- and triphosphate groups: $Cs(MoO)_4(P_2O_7)_2(P_3O_{10})$
André Leclaire and Bernard Raveau
Page 2433

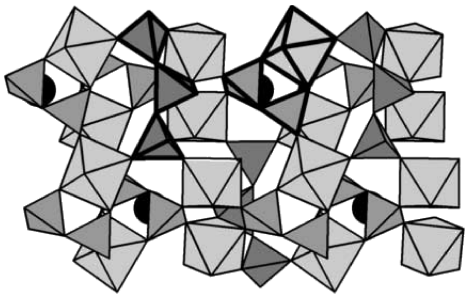

The structure of $Cs(MoO)_4(P_2O_7)_2(P_3O_{10})$ viewed along **a** with one P_3O_{10} group and one MoP_2O_{11} unit headlined.

First-principles relativistic calculation for 4*f*–5*d* transition energy of Ce^{3+} in various fluoride hosts
Shinta Watanabe, Takugo Ishii, Koji Fujimura and Kazuyoshi Ogasawara
Page 2438

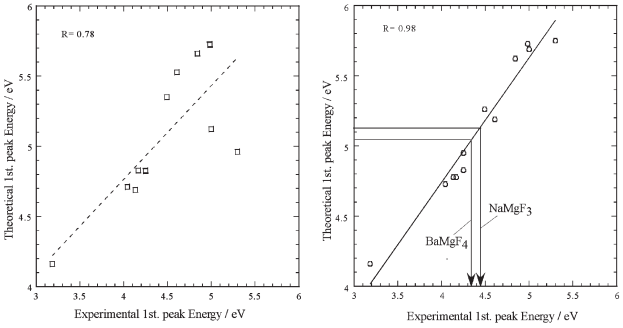

Correlation diagram between the experimental 1st peak energy and the theoretical 1st peak energy. The left figure (A) shows the results without the lattice relaxation by correction of bond length and right one (B) shows the results with the lattice relaxation by correction of bond length. The corresponding coefficients of correlation *R* are 0.78 and 0.98, respectively.

Phase coexistence in $CaCu_xMn_{7-x}O_{12}$ solid solutions
W. Sławiński, R. Przeniosło, I. Sosnowska, M. Bieringer, I. Margiolaki, A.N. Fitch and E. Suard
Page 2443

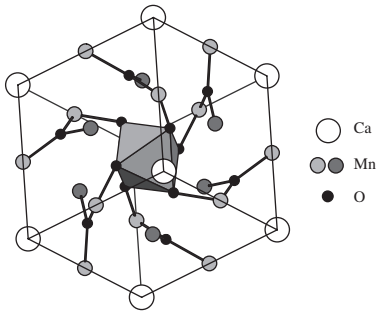

Schematic representation of the trigonal $CaCu_xMn_{7-x}O_{12}$ unit cell shown in the rhombohedral setting of space group $R\bar{3}$.

Continued

A one-step solvothermal route for the synthesis of nanocrystalline anatase TiO_2 doped with lanthanide ions
Daniele Falcomer, Matteo Daldosso, Carla Cannas, Anna Musinu, Barbara Lasio, Stefano Enzo, Adolfo Speghini and Marco Bettinelli
Page 2452

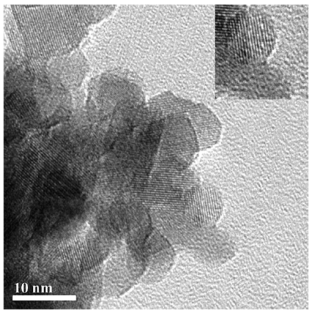

HRTEM image of Eu^{3+} doped anatase TiO_2 nanocrystalline powders prepared by a solvothermal technique.

Selective substitution of vanadium for molybdenum in $Sr_2(Fe_{1-x}V_x)MoO_6$ double perovskites
Q. Zhang, G.H. Rao, Q. Huang, X.M. Feng, Z.W. Ouyang, G.Y. Liu, B.H. Toby and J.K. Liang
Page 2458

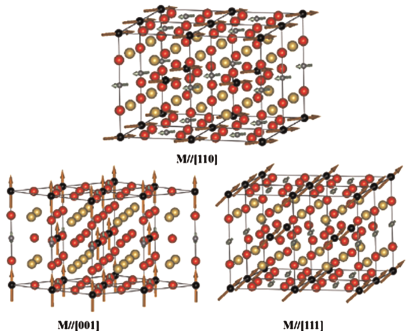

Magnetic structure models with the moments aligning along [110], [100] and [111] directions, respectively, for $Sr_2(Fe_{1-x}V_x)MoO_6$ compounds.

Synthesis, crystal structure and charge distribution of $Na_7As_{11}O_{31}$: An oxygen-deficient layered sodium arsenate
Abderrahmen Guesmi, Massimo Nespolo and Ahmed Driss
Page 2466

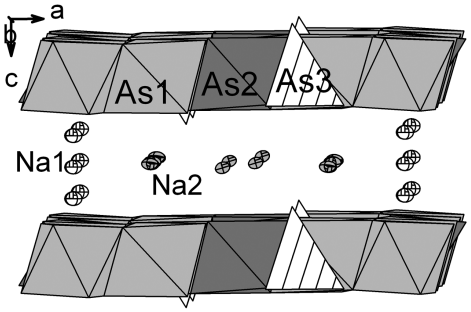

Perspective view of the layer structure of the oxygen-deficient sodium arsenate $Na_7As_{11}O_{31}$.

Preparation, crystal structure and chemical bonding analysis of the new binary compounds Rh_4Ga_{21} and Rh_3Ga_{16}
Magnus Boström, Yurii Prots and Yuri Grin
Page 2472

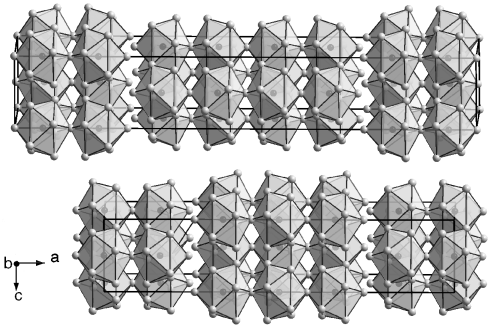

Crystal structures of Rh_4Ga_{21} and Rh_3Ga_{16}.

The mercury chromates $Hg_6Cr_2O_9$ and $Hg_6Cr_2O_{10}$—Preparation and crystal structures, and thermal behaviour of $Hg_6Cr_2O_9$
Matthias Weil and Berthold Stöger
Page 2479

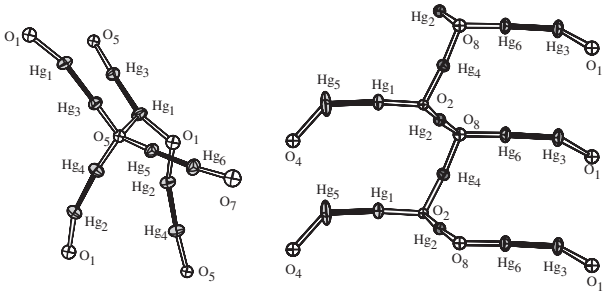

$Hg_6Cr_2O_9$ (left) and $Hg_6Cr_2O_{10}$ (right): details of the Hg–O network.

Synthesis, structures and phase transitions in the double perovskites $Sr_{2-x}Ca_xCrNbO_6$
Melina C.L. Cheah, Brendan J. Kennedy, Ray L. Withers, Masao Yonemura and Takashi Kamiyama
Page 2487

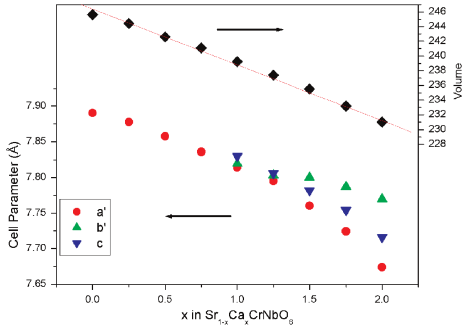

Variation of the lattice parameters and volume in the series $Sr_{2-x}Ca_xCrNbO_6$. The lattice parameters in the monoclinic phase have been scaled for ease of comparison. The solid line is a linear fit to variation in volume.

Local crystal chemistry, structured diffuse scattering and the dielectric properties of $(Bi_{1-x}Y_x)_2(M^{III}Nb^{V})O_7$ ($M = Fe^{3+}$, In^{3+}) Bi-pyrochlores

W. Somphon, V. Ting, Y. Liu, R.L. Withers, Q. Zhou and B.J. Kennedy

Page 2495

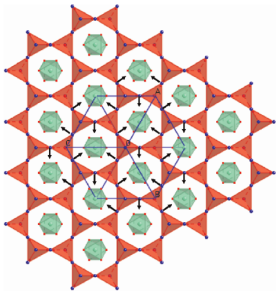

The pattern of correlated O′Bi_4 tetrahedral rotation around the ⟨111⟩ axis responsible for the observed ⟨111⟩* rods of diffuse intensity in Bi-pyrochlores.

Preparation, structural study from neutron diffraction data and magnetism of the disordered perovskite $Ca(Cr_{0.5}Mo_{0.5})O_3$

M.J. Martínez-Lope, J.A. Alonso, M.T. Casais, M. García-Hernández and V. Pomjakushin

Page 2506

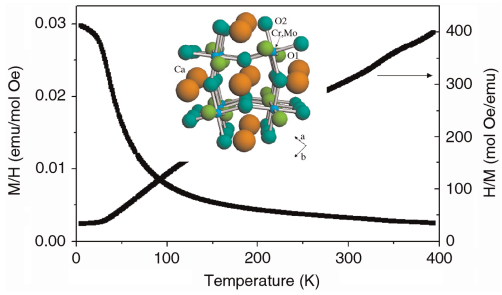

$Ca(Cr_{0.5}Mo_{0.5})O_3$ is orthorhombic, *Pbnm* space group, and exhibits a complete disordering of Cr^{3+} and Mo^{5+} over the *B*-site of the perovskite. The magnetic susceptibility is characteristic of a ferrimagnetic behavior, with $T_C = 125$ K, and a small saturation magnetization at $T = 5$ K, of 0.05 μ_B/f.u.

Properties of cerium–zirconium mixed oxides partially substituted by neodymium: Comparison with Zr–Ce–Pr–O ternary oxides

Jana Mikulova, Sylvie Rossignol, Francois Gérard, Danielle Mesnard, Charles Kappenstein and Daniel Duprez

Page 2511

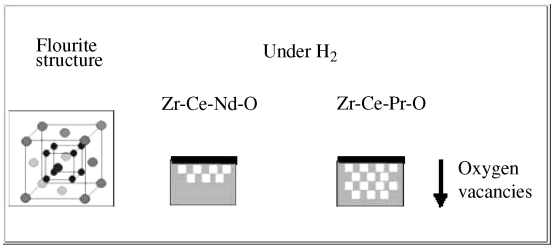

Variation of oxygen vacancies under hydrogen on ternary oxides.

Unusual supramolecular assembly and nonlinear optical properties of L-histidinium hydrogen malate

E. de Matos Gomes, V.H. Rodrigues, M.M.R. Costa, M.S. Belsley, P.J.M. Cardoso, C.F. Gonçalves and F. Proença

Page 2521

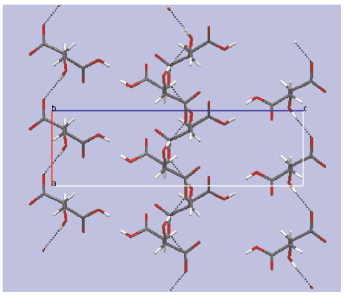

One-dimensional malate chains running along [100]. The anions form head-to-side chains where the COO^- group of one anion is hydrogen bonded to the COH side group of a neighbor one.

Controlled peak wavelength shift of $Ca_{1-x}Sr_x(S_ySe_{1-y}):Eu^{2+}$ phosphor for LED application

Mihail Nazarov and Chulsoo Yoon

Page 2529

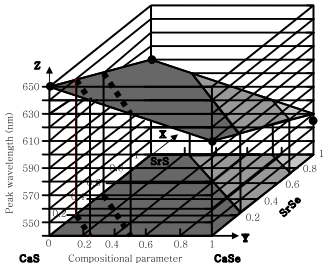

Peak wavelength diagram for $(Ca_{1-x}Sr_x)(S_{1-y}Se_y):Eu^{2+}$.

A series of borate-rich metalloborophosphates $Na_2[M^{II}B_3P_2O_{11}(OH)]\cdot 0.67H_2O$ (M^{II} = Mg, Mn, Fe, Co, Ni, Cu, Zn): Synthesis, structure and magnetic susceptibility

Tao Yang, Guobao Li, Jing Ju, Fuhui Liao, Ming Xiong and Jianhua Lin

Page 2534

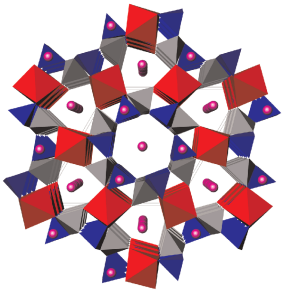

A series of metalloborophosphates $Na_2[M^{II}B_3P_2O_{11}(OH)]\cdot 0.67H_2O$ (M^{II} = Mg, Mn, Fe, Co, Ni, Cu, Zn) were synthesized under hydrothermal conditions (473 K). The structure consists of microporous 3D open framework with 12-membered ring channels composed of octahedral ($M^{II}O_6$), tetrahedral (BO_4, PO_4) and triangular ($BO_2(OH)$) units.

Continued

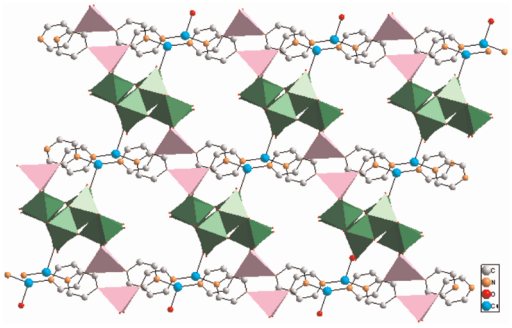

A novel three-dimensional framework constructed from ξ-octamolybdate chains integrated by pairs of 1D copper-quinoxaline polymer chains.

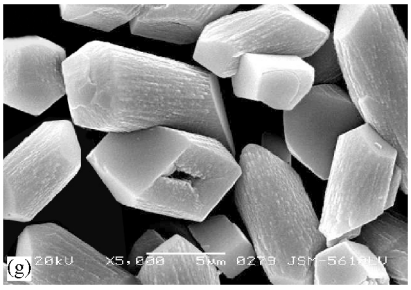

Pure calcite crystal with different morphologies such as wood-block and spherical aggregates were prepared by a simple precipitation reaction in the presence of citric acid and the formation mechanism was proposed.

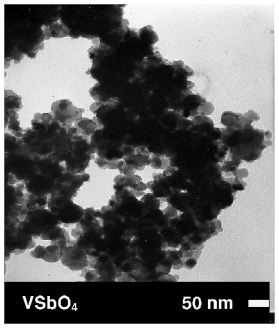

TEM image of nanosized $VSbO_4$ sample.

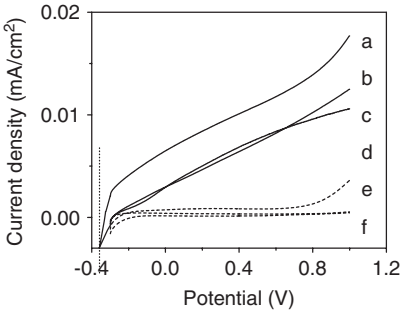

Current vs. potential curves for $ZnWO_4$ film treated at various temperatures: ((a) photo 500 °C; (b) photo 550 °C; (c) photo TiO_2; (d) dark 500 °C; (e) dark 550 °C; (f) dark TiO_2) in 0.5 M Na_2SO_4 solution pH 6.0, scan rate = 10 mV s^{-1}.

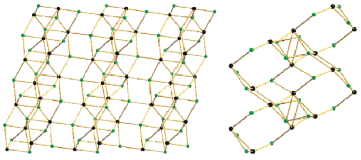

Two lanthanum phosphites, $La_2(H_2O)(HPO_3)_3$ (**1**) and $La_2(H_2O)_2(HPO_3)_3$ (**2**), were synthesized by modified hydrothermal methods and their crystal structures showed different arrangements of face-sharing dimers of La coordination polyhedron observed for the first time in rare-earth phosphites. The two Ce^{+3}-doped compounds show intensive broad emission band around 340 nm under UV excitation.

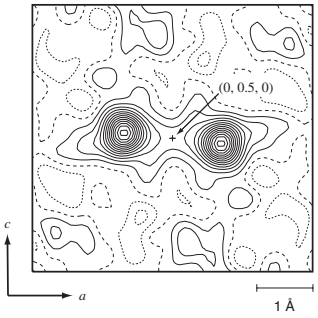

Difference Fourier map at the $y = 0.5$ section for $Na_2Cr_2Ti_6O_{16}$ with a structure model containing no Na ions.

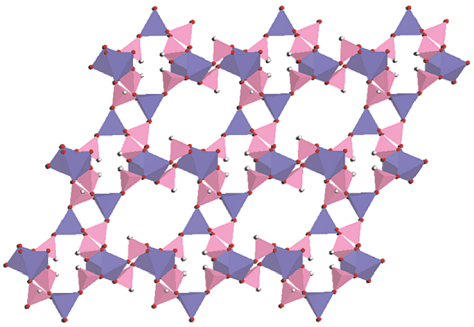

View of the 3-D structure along the *a*-axis.

SEM image of $SrAl_{12}O_{19}$:Eu.

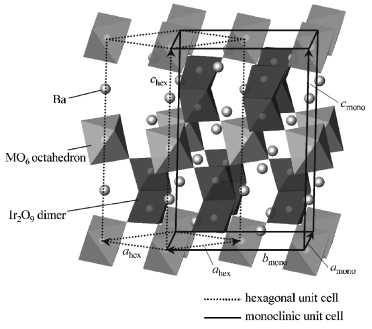

The schematic crystal structure of $Ba_3MIr_2O_9$. Among the title compounds, only $Ba_3M^{3+}Ir_2^{4.5+}O_9$ (M = Sc, In) show an antiferromagnetic transition at low temperatures.

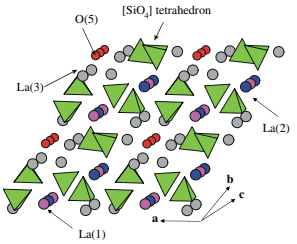

Crystal structure of lanthanum silica apatite.

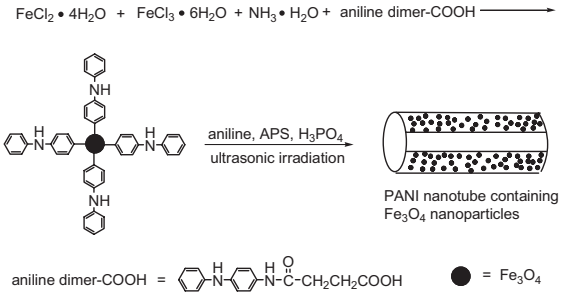

Simplified schematic representation of the preparation of PANI/Fe_3O_4 composite nanotubes assisted by ultrasonic irradiation.

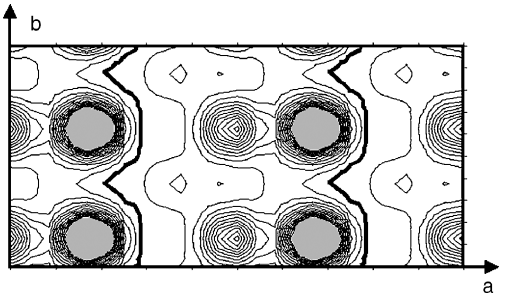

Bond-valence map for Li in $Na_{0.7}Li_{0.7}[V_3O_8]$. Contour lines representing the bond-valence sum of 1.0 vu are marked with thick black lines and indicate potential diffusion pathways of Li.

Continued

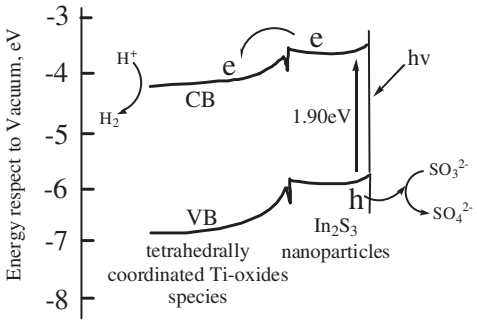

Proposed band energy diagram for In_2S_3@Ti-MCM-41 in an aqueous Na_2SO_3 solution (pH = 8.8).

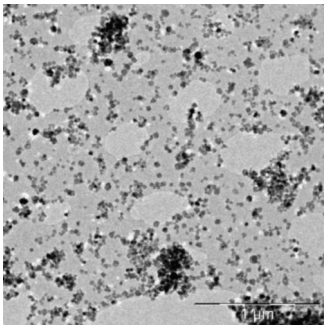

Transmission Electron Microscopy micrograph of CaF_2 nanoparticles synthesized by a reverse-micelle method.

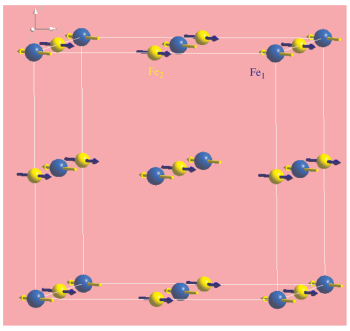

Magnetic structure of the oxygen-deficient perovskite $Ba_3Fe_2WO_{8.45}$.

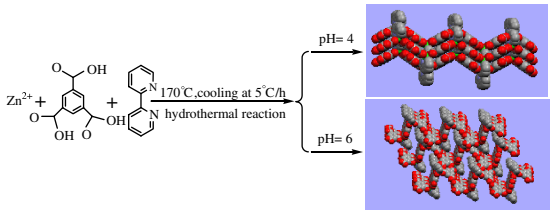

The schematic representation highlighting the pH-dependent formation in the synthesis processes of a pair of isomers.

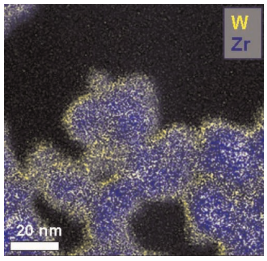

WO_x–ZrO_2 catalysts were obtained by precipitating zirconium oxynitrate in presence of $WO_4^{=}$ species. Initially, the W atoms remained inside the crystallite after annealing at 560 °C in a reduced oxidation state (W^{5+}), whereas, the sample annealed at 800 °C, the W atoms migrate from the bulk to the surface, forming a layer of W atoms on a ZrO_2 core, with the consequent oxidation to W^{6+}, producing patches of nanocrystalline WO_3 with dimension smaller than 3 nm.

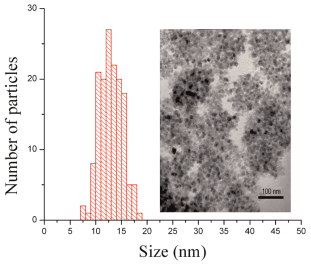

The synthesis parameter space (T, P, concentration) for supercritical synthesis of TiO_2 in a propanol–water mixture has been explored, and the nanocrystalline products comprehensively characterized.

Structural transformations in the $Na_{4+x}VO(PO_4)_2$ vanadylphosphates

Roman V. Shpanchenko, Evgeny V. Dikarev, Andrey V. Mironov, Svetlana N. Mudretsova and Evgeny V. Antipov

Page 2681

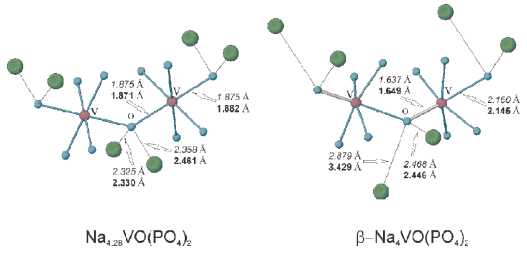

Bond valence calculations have been used to explain the charge redistribution between vanadium atoms in neighboring chains in the $Na_{4+\delta}VO(PO_4)_2$ structures.

Crystal structures and phase stability in pseudobinary $CaAl_{2-x}Zn_x$

Karin Söderberg, Magnus Boström, Yoshiki Kubota, Takeshi Nishimatsu, Rainer Niewa, Ulrich Häussermann, Yuri Grin and Osamu Terasaki

Page 2690

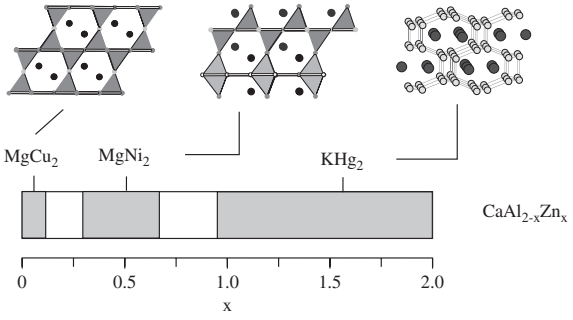

The investigation of the pseudobinary system $CaAl_{2-x}Zn_x$ yielded the structural sequence $MgCu_2$ (C15)–$MgNi_2$ (C36)–KHg_2 with increasing x. The structural change C15→C36 between two Laves phase structures is induced by the decrease in valence electron concentration. However, with increasing Zn content the system becomes increasingly polar and at some point favours the more open packed KHg_2 structure over a Laves phase structure.

Fabrication and optical properties of core–shell structured spherical SiO_2@$GdVO_4$:Eu^{3+} phosphors via sol–gel process

Guangzhi Li, Zhenling Wang, Min Yu, Zewei Quan and Jun Lin

Page 2698

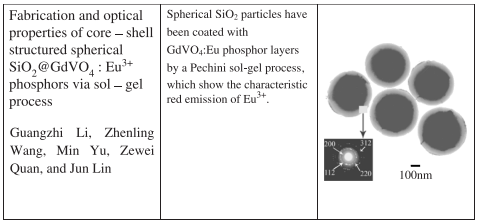

Spherical SiO_2 particles have been coated with $GdVO_4$:Eu phosphor layers by a Pechini sol–gel process, which show the characteristic red emission of Eu^{3+}.

Crystal structure, electronic structure and physical properties of the new low-valent thallium silicon telluride $Tl_6Si_2Te_6$ in comparison to $Tl_6Ge_2Te_6$

Abdeljalil Assoud, Navid Soheilnia and Holger Kleinke

Page 2707

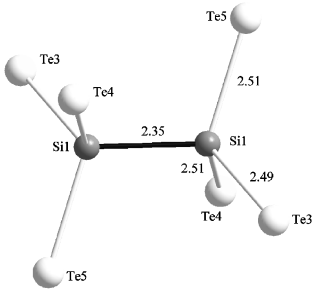

The isostructural tellurides $Tl_6Si_2Te_6$ and $Tl_6Ge_2Te_6$ contain Si^{III} and Ge^{III} in dimeric $[Si_2Te_6]^{6-}$ and $[Ge_2Te_6]^{6-}$ units, respectively. Both materials are black semiconductors with high Seebeck coefficients and reasonable electrical conductivities, despite their molecular character.

Electron-irradiation induced phase transformation in $La_{1/3}Zr_2(PO_4)_3$: La^{3+} displacement in a preserved NASICON framework

M.P. Crosnier-Lopez, M. Barre, F. Le Berre and J.L. Fourquet

Page 2714

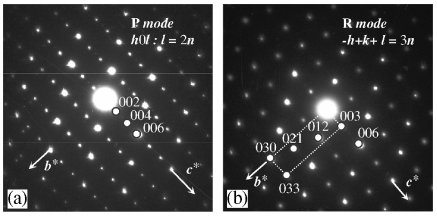

Diffraction pattern of a crystallite of $La_{1/3}Zr_2(PO_4)_3$ showing the transformation under the electron beam (a) at the beginning and (b) at the end.

Thermodynamic properties of complex oxides in the La–Ni–O system

D.O. Bannikov and V.A. Cherepanov

Page 2721

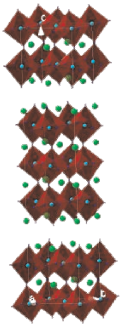

The crystal structure of $La_4Ni_3O_{10}$.

Continued

Rapid Communications

Low temperature synthesis of bilayer hydrated cesium cobalt oxide

Horng Y. Tang, Hsiao Y. Lin, Ming J. Wang, Ming Y. Liao, Fon C. Hsu, Boon H. Mok, Jean L. Liu, Michael T. Beasley, Hwo S. Sheu and Maw K. Wu

Page 2728

BLH $Cs_{0.2}CoO_2 \cdot 0.63H_2O$ crystals grown from low temperature molten salt.

"Unusual" phase transitions in $CeAlO_3$

W.T. Fu and D.J.W. IJdo

Page 2732

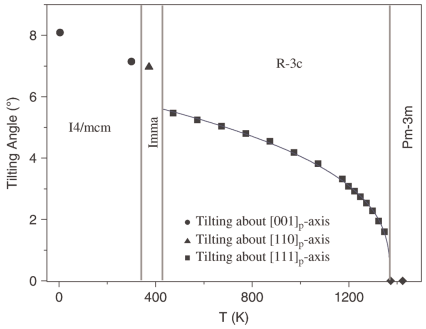

Temperature dependence of the octahedral tilting angles in $CeAlO_3$. The continuous line in rhombohedral phase region is the fit to the expression: $\phi = A(T_c - T)^{\beta}$ with fitted values of $T_c = 1371$ K, $\beta = 0.35$ and $A = 0.52$. Note that the lines that separate the $I4/mcm$ and $Imma$ phases and the $Imma$ and $R\bar{3}c$ phases are not experimentally determined transition temperatures but for visualisation purpose.

Pressure-induced polymorphism in Al_3BC_3: A first-principles study

Jingyang Wang, Yanchun Zhou, Zhijun Lin and Ting Liao

Page 2739

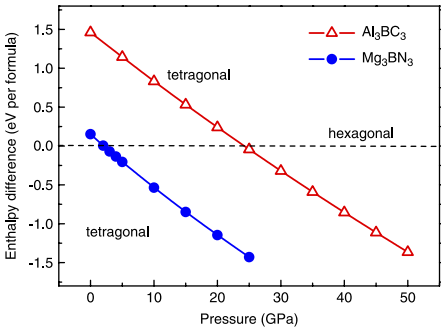

Relative enthalpy of tetragonal phase with respect to hexagonal phase at various pressures. The pressure-induced phase transformation occurs at about 2 and 24 GPa for Mg_3BN_3 and Al_3BC_3, respectively.

NOTICE

The Keyword Index for Volume 179 will appear in the December 2006 issue as part of a cumulative index for the year 2006.